ELSEVIER

Contents lists available at ScienceDirect

# **Materials Characterization**

journal homepage: www.elsevier.com/locate/matchar



# Discontinuous grain growth in an equal-channel angular pressing processed Fe-9Cr steel with a heterogeneous microstructure



Jiaqi Duan<sup>a</sup>, Haiming Wen<sup>a,b,\*</sup>, Caizhi Zhou<sup>a</sup>, Xiaoqing He<sup>c,d</sup>, Rinat Islamgaliev<sup>e</sup>, Ruslan Valiev<sup>e,f</sup>

- <sup>a</sup> Department of Materials Science and Engineering, Missouri University of Science and Technology, Rolla, MO, 65409, USA
- b Department of Ming and Nuclear Engineering, Missouri University of Science and Technology, Rolla, MO, 65409, USA
- <sup>c</sup> Electron Microscopy Core Facilities, University of Missouri, Columbia, MO, 65211, USA
- <sup>d</sup> Department of Mechanical and Aerospace Engineering, University of Missouri, Columbia, MO, 65211, USA
- e Institute of Physics of Advanced Materials, Ufa State Aviation Technical University, Ufa, 450008, Russia
- <sup>f</sup> Saint Petersburg State University, Universitetskiy prospekt, 28, Peterhof, St, Petersburg, 198504, Russia

#### ARTICLE INFO

#### Keywords: ECAP Microstructure Grain growth Textures Steel Thermal stability

#### ABSTRACT

A particle-containing Fe-9Cr steel was processed by six passes of equal-channel angular pressing (ECAP) using route Bc to produce an ultrafine-grained (UFG) microstructure with a heterogeneous distribution of high-angle boundaries (HABs) and low-angle boundaries (LABs). Annealing was carried out on the ECAP-processed Fe-9Cr from 500 to 700 °C, for up to 48 h. It was found that the UFG microstructure was stable up to 550 °C. Discontinuous grain growth was first observed in the sample annealed at 600 °C, accompanied by an increase in LAB fraction. The discontinuous grain growth became evident during high temperature annealing (650–700 °C), leading to a reduction in LAB fraction and a significant increase in grain size. Grain growth was the main reason for the decline in hardness. It is proposed that in the current heterogeneous microstructure, grain growth initially occurs in regions of dominantly HABs, and subsequently takes place in regions that mainly consist of LABs, thereby forming a bimodal microstructure. Textures of the annealed structure were shown to be similar to those of the ECAP processed structure. No differences in textures were found between abnormal grains and the matrix in the annealed structure in current case.

## 1. Introduction

Severe plastic deformation (SPD) is a well-known top-down procedure to achieve extreme grain refinement while still maintaining the dimensions of the bulk materials [1-4]. Many properties greatly benefit from grain refinement, including strength, fatigue resistance, toughness, and irradiation resistance. For example, the strength of ultrafinegrained (UFG,  $100 \text{ nm} < \text{grain size} < 1 \mu\text{m}$ ) and nanocrystalline (NC, grain size < 100 nm) metals is typically at least several times that of their coarse-grained (CG, grain size  $> 1 \mu m$ ) counterparts. UFG and NC materials generally contain high amounts of stored energy in dislocations and grain boundaries, providing a driving force for grain growth [5–8]. In addition, grain boundaries formed during SPD are believed to be in a non-equilibrium state, which can have higher mobility [9,10]. Therefore, UFG or NC materials are expected to show faster restoration than their CG counterparts. Generally, UFG or NC metals produced by SPD typically have limited ductility compared to their CG counterparts, owing to the high dislocation density and very small grain size [2]. Consequently, annealing is often performed after SPD to restore some ductility. The study of microstructure evolution during the annealing of UFG and NC materials is of considerable interest, since it provides information about the thermal stability of microstructures and offers guidelines for thermomechanical processing to achieve a balance between high strength and acceptable ductility in such materials.

The literature has shown that the microstructural evolution of a UFG structure during annealing can be affected by factors such as grain boundary characteristics, precipitates, and textures. It has been reported that the microstructure with a high fraction of LABs showed exceptional thermal stability, since LABs have much lower mobility than HABs [11,12]. Boundary characteristics also decide whether grain growth occurs in a continuous or discontinuous manner. Humphreys showed that continuous grain growth prevails when the HAB fraction exceeds 0.7 [13,14]. However, a UFG structure starting with a HAB fraction over 0.7 can also have discontinuous grain growth if it has strong textures [15,16]. This is because new LABs can form when two grains of similar orientation encounter each other during growth (termed "orientation impingement"), leading to a decrease in the HAB fraction. Furthermore, second-phase particles in UFG materials can play

<sup>\*</sup> Corresponding author. Department of Materials Science and Engineering, Missouri University of Science and Technology, Rolla, MO, 65409, USA. E-mail address: wenha@mst.edu (H. Wen).

a significant role during annealing. Smaller particle size and higher particle volume fraction lead to larger Zener pinning, hence slower grain growth rate and smaller critical grain size at which grain growth stops [17]. In addition, grains are predicted to grow in a more discontinuous manner, i.e. resulting in broader grain size distribution, as Zener pinning increases [18]. With appropriate annealing of UFG materials, bimodal grain-sized microstructure can be obtained most likely through discontinuous grain growth. Materials consisting of bimodal grain-sized structure are reported to exhibit a good combination of high strength and high ductility [19,20]. However, there lacks the information on how this kind of structures were developed during annealing.

Fe-9Cr steel is the leading fuel cladding and structural material for advanced fast reactors and, potentially, for light water reactor core internals [21]. Equal-channel angular pressing (ECAP), an innovative and low-cost SPD technique, was applied to Fe-9Cr to produce an UFG heterogeneous microstructure [22,23]. As previous studies of annealing behaviors mainly focus on homogenous microstructures with random distribution of HABs and LABs [14,16,24], ECAP processed Fe-9Cr provides an opportunity to study annealing behaviors in the heterogeneous microstructure during annealing. In this work, thermal stability study was carried out on an ECAP processed Fe-9Cr steel to reveal how the heterogeneities affected the microstructure evolution and to understand how a bimodal grain-sized structure was developed in this steel during restoration process. Electron backscatter diffraction (EBSD) and transmission electron microscopy (TEM) were performed to determine the evolution of its microstructure and texture during annealing. X-ray diffraction (XRD) was conducted to estimate the dislocation density of selected samples.

#### 2. Experimental

A hot rolled Grade 91 (G91) steel was used with the following composition: Fe–8.38Cr–0.9Mo–0.2V–0.06Nb–0.17Ni-0.43Mn-0.1C–0.03N (in wt.%). The "as-received" rods were normalized at 1050 °C for 1 h and quenched in oil, followed by tempering at 800 °C for 1 h, and then air cooling. The rods (25 mm in diameter and 100 mm in length) were processed by ECAP at 300C for six passes, with a 90-degree rotation between passes (route Bc) [25]. The ECAP die had an outer corner angle of  $\psi=0$ ° and an intersection angle of  $\varphi=120$ °. The amount of total equivalent strain imposed to the samples was calculated to be  $\sim$ 3.6. Subsequent annealing was carried out on the ECAP processed samples at 500 °C–700 °C, up to 48 h, in a tube furnace. Samples were cooled in the furnace.

Hardness changes after annealing were measured using Vickers's microhardness with eight measurements for each condition. The load force and holding time were 4.9 N and 15s, respectively. Microstructural analyses, after ECAP and subsequent annealing, were performed using TEM and EBSD. TEM samples were prepared by mechanical grinding, followed by dimpling and ion milling. TEM was carried out using a FEI TEM operating with a 200 KeV electron beam. EBSD samples were prepared by mechanical polishing, using 0.02 μm colloidal silica for the final polishing stage. EBSD scans were carried out using an Oxford EBSD system interfaced to a Helios Nanolab scanning electron microscope (SEM). The principal directions of the ECAP are denoted as the extrusion direction (ED), transverse direction (TD) and normal direction (ND). The crystallographic information of a microstructure was determined by using HKL Channel 5. The crystallographic boundaries were classified based on their misorientations, i.e., > 15° misorientations for high-angle boundaries (HABs, denoted in black in EBSD orientation maps), and 2-15° misorientations for low-angle boundaries (LABs, denoted in red in EBSD orientation maps).

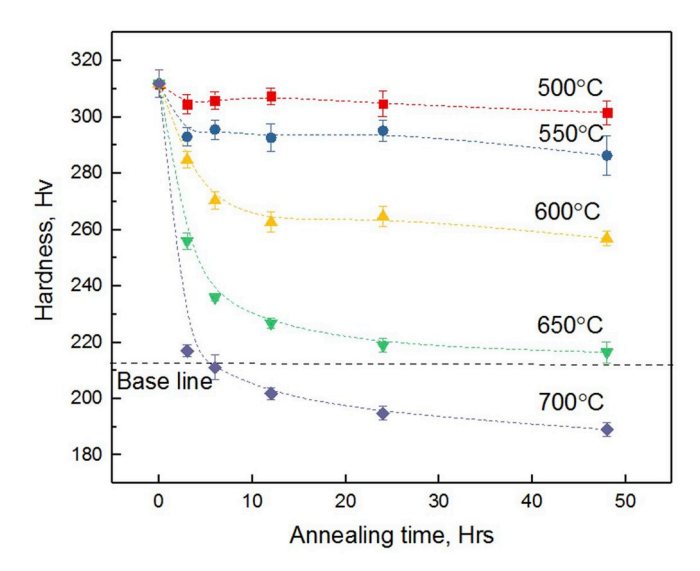


Fig. 1. Vickers's hardness changes in the ECAP-processed Fe-9Cr alloy after annealing at various temperatures for up to 48 h. Base line indicates the hardness before ECAP.

#### 3. Results

#### 3.1. Microhardness

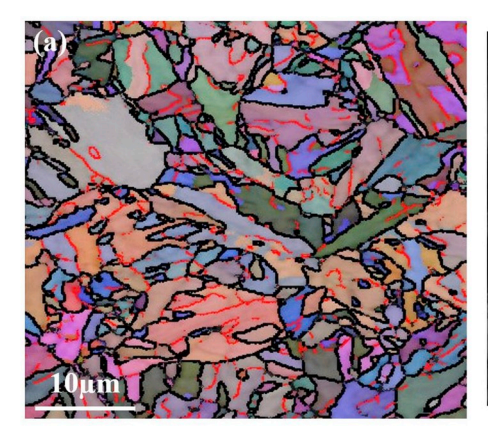
Vickers's microhardness, as a function of annealing time at various annealing temperatures, is displayed in Fig. 1. Microhardness before ECAP processing was 190 Hv, and increased to 313Hv after six passes of ECAP. Annealing at lower temperatures (500 °C–550 °C) only led to a slight decrease in hardness during the first few hours. As annealing continued, hardness remained relatively stable. At higher annealing temperatures (650 °C–700 °C), hardness decreased dramatically during the first few hours, and kept decreasing as annealing time was extended. Hardness lower than that of the CG sample was observed for samples annealed at 700 °C for over 6 h.

## 3.2. Initial microstructure

For the CG Fe-9Cr steel, after normalization and tempering, a ferritic microstructure is observed, which consists of microscale laths and block grains with a high density of dislocations, Fig. 2a-b. The CG Fe-9Cr steel sample contains two main types of secondary precipitates at grain boundaries and in the grains, i.e.,  $M_{23}C_6$  and MX, where M and X denote metallic elements and carbon and/or nitrogen, respectively.  $M_{23}C_6$  precipitates are enriched in Cr and Mo, and MX precipitates are enriched in Nb and V.

## 3.3. Deformation microstructure

The EBSD orientation map (Fig. 3a) of the cross-section of the ECAP-processed sample shows a microstructure consisting of lath-shaped as well as near-equiaxed grains in sub-micron size, which agrees with the microstructure reported for other ECAP-processed metals using the Bc route [26]. The average grain size is 310 nm. It is worth noting that clusters of subgrains with LABs, marked A, co-exist with regions of grains with HABs, marked B. The corresponding (110) pole figures (PF) in Fig. 3b-c shows the orientation distribution of region A and B, respectively. A large spread in orientation is observed in region B, while the orientations are clustered in region A. The misorientation distribution profile, Fig. 3d, exhibits bimodal boundary distribution with a



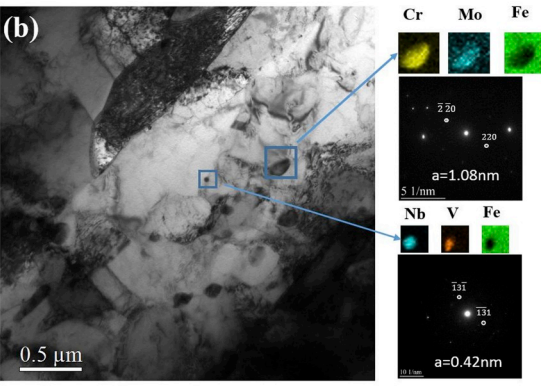


Fig. 2. (a) EBSD orientation map of a normalized and tempered Fe-9Cr alloy showing grains of a few micrometers; (b) TEM image coupled with EDS maps and selected-area diffraction pattern displaying two types of precipitates that exist in the Fe-9Cr alloy:  $M_{23}C_6$  enriched in Cr and Mo (face-centered cubic structure (fcc) with a lattice parameter a of 1.08 nm) and MX enriched in Nb and V (fcc, a = 0.42 nm).

peak at low angles (below 15°) and another one at high angles (close to 55°). The fraction of LAB is 0.41. EBSD scans taken from the longitudinal section show identical microstructure, which is anticipated when samples are processed using route Bc during ECAP. Accordingly, results from the longitudinal session are not given here. The TEM image of the ECAP-processed Fe-9Cr, Fig. 3e, shows a UFG microstructure with  $\rm M_{23}C_6$  and MX precipitates. After ECAP, the distribution of the precipitates seems to be random. In order to estimate statistics for the secondary precipitates, EDS scans of a large area of the TEM sample were made (Fig. S1). Precipitates rich in Cr and Mo are considered  $\rm M_{23}C_6$ , and those rich in V and/or Nb are considered MX. Analyses show the average radius of  $\rm M_{23}C_6$  and MX precipitates as 56 and 20 nm, respectively, and the fraction of  $\rm M_{23}C_6$  and MX as 2.2% and 0.3%, respectively.

#### 3.4. Annealing microstructure

Fig. 4 a-d show the microstructure of the ECAP-processed Fe-9Cr that was annealed for 48 h at various temperatures. The corresponding average grain sizes, determined by linear interception (critical misorientation angle is 2°), are given in Fig. 4e. When annealed at 500 and 550 °C, the average grain size slightly increased. Nevertheless, the microstructure still resembles that of the as-ECAP sample (Fig. 4a). For the 600 °C annealed sample, grains noticeably larger than the neighboring grains are occasionally found. In addition, those grains show homogenous orientation inside them, as revealed by the accumulative misorientation profile, indicating that restoration was completed in those grains. The presence of those grains provides evidence for the onset of discontinuous grain growth. Regarding the sample annealed at 650 °C (Fig. 4c), abnormally large grains (4–20 μm in diameter) occupies 35% of the area, while the rest of the grains have an average size of  $0.77 \, \mu m$ , which constitute a heterogeneous microstructure. At 700 °C (Fig. 4d), discontinuous grain growth became even more evident, and the average grain size significantly increased to  $1.2\,\mu m$ , as compared to  $310\,nm$  in as-ECAP condition. The area fraction of large grains increased to 37%. It is interesting to note that the grain boundaries of abnormal grains are predominantly HABs, while the rest of the regions contain a high fraction of LABs. A comparison of grain-size distribution between the as-ECAP and 700°C-annealed samples (Fig. 5) indicates that discontinuous grain growth led to: 1) significant broadening in grain size distribution; and 2) bimodal grain size distribution. This would be promising for achieving a good balance between ductility and strength for UFG metals and alloys [20]. Briefly, in bimodal grain sized materials, in addition to the strengthening from small grains (hard domain) due to Hall-Petch relationship, the large grains (soft domain) can contribute extra strength during deformation due to the pile-up of geometrically necessary dislocations (GNDs) at their boundaries, leading to a high global strength. Meanwhile, to accommodate the deformation, the strain gradients between the large (soft) and small (hard) grains are generated, and the resultant back-stress work hardening can help to prevent necking and improve ductility [19].

EDS mappings of the TEM sample, subjected to annealing for 48 h at 700 °C, Fig. S2, show the average size of  $M_{23}C_6$  and MX precipitates to be 85 and 21 nm, respectively. Compared to the precipitate sizes measured in the as-ECAP sample, it is concluded that  $M_{23}C_6$  coarsened, while MX precipitates were relatively stable during annealing.

Fig. 6 shows EBSD orientation maps of the samples annealed for various hours at 650 °C to illustrate microstructure evolution during discontinuous grain growth. After 3 h of annealing, grains ~3–5 times larger than surrounding grains appeared, similar to what were observed in the sample annealed for 48 h at 600 °C. As annealing proceeded, large grains grew by invading the surrounding small (sub) grains. After 12 h of annealing, abnormally large grains developed and were often connected to other abnormal grains. The average grain size as a function of annealing time, Fig. 6d, shows a rapid increase in grain size during the first 12 h, but a much slower increase thereafter.

It is also observed that the LAB fraction increased during lower temperature annealing. The LAB fraction was 0.41 in the as-ECAP condition (Fig. 3a), and the value increased to 0.48 (Fig. 7a), after annealing at 600 °C for 48 h. A decrease in the fraction of LAB was seen when the annealing temperature was above 650 °C. After annealing for 48 h at 700 °C, the LAB fraction dropped to 0.3 (Fig. 7b). During isothermal annealing at 650 °C, the LAB fraction increased during the first few hours, but decreased thereafter, as indicated in Fig. 7c–e.

## 3.5. Texture

Texture development during ECAP is complex due to high-strain deformation and strain path changes. The textures in ECAP-processed metals are often correlated to the simple shear textures because simple shearing is considered as the deformation mode in ECAP. The ideal ECAP textures are derived from those for simple shear by a counterclockwise rotation around TD by angle  $\Phi/2$ , where  $\Phi$  is the angle between the two channels [27,28]. Fig. 8 shows the (110) pole figure (PF) map of the as-ECAP Fe-9Cr and Fe-9Cr annealed at 700 °C for 48 h. Note that it was very difficult to determine the exact TD and ND of the ECAP rod since the cylindrical geometry caused inaccuracies relative to the TD and ND during processing and sample preparation. Therefore, texture information displayed on PF is approximate. Nevertheless, it is still clear that orientation distributions were unsymmetrical and spread, and that ideal shear textures, i.e. partial {110} and < 111 > fiber [27], were not fully developed after six passes of ECAP with a total strain of 3.6. Although a high strain was imposed, the material displayed relatively diffuse textures, which could be attributed to the strain path changes involved in the processing [29]. However, the formation of partial {110} and < 111 > fiber can still be verified in the PF. The results in Fig. 8a agrees with the textures reported for interstitial-free steel ECAP-processed to similar strains using the Bc route [26].

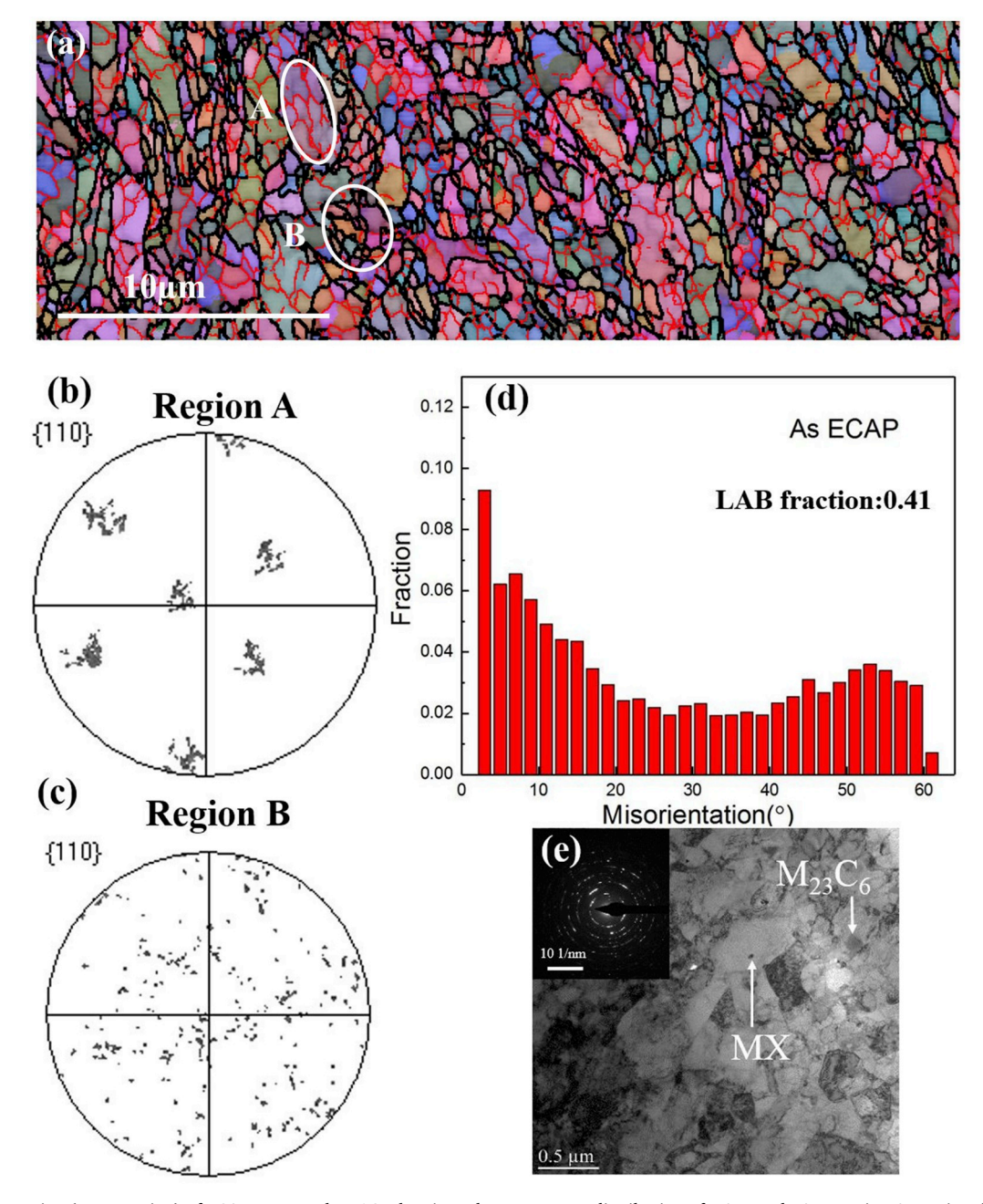


Fig. 3. (a) EBSD mapping (cross section) of ECAP processed Fe-9Cr showing a heterogeneous distribution of HABs and LABs; region A consists dominantly of LABs with clustered orientations (b), while region B consists dominantly of HABs with a large spread of orientations (c); (d) bimodal distribution of the misorientation in ECAP processed Fe-9Cr; (e) TEM image showing UFG structure and two types of precipitates  $M_{23}C_6$  and MX.

It is also interesting to note that the 700 °C 48h annealed sample (Fig. 8b) shows a similar texture skeleton as that in Fig. 8a. This suggests that there was no obvious change in textures after annealing, despite significant changes in the microstructure. To ascertain whether there was any preferred growth of grains with particular textures, the PF of those abnormally large grains with an area larger than  $20\,\mu\text{m}^2$  were plotted and compared to that of the rest of the grains.  $20\,\mu\text{m}^2$  was chosen as the threshold for grain area, as this value was between the two peaks in the bimodal size distribution. It is observed that textures of the large grains are similar to those of the smaller grains, suggesting no growth advantage for any particularly orientated grains. The observation here is unique, when compared to previous annealing texture studies of severely deformed metals. It is common to observe preferred growth of grain in certain texture components in severely deformed metals during annealing, leading to the strengthening of these textures

in the restored structure. For interstitial-free Fe subjected to accumulative rolling, grains in {h11} < 1/h 1 2 > showed growth advantage during restoration process and {h11} < 1/h 1 2 > texture component was accordingly strengthened [30]. For the high-pressure torsion (HPT) processed Fe-9Cr steel, grains in {110} < 112 > grew faster than grains in other orientations and resultantly {110} < 112 > became the dominant texture after restoration [31]. However, in current work, no preferred growth of grains with particular texture is detected.

# 4. Discussion

#### 4.1. Microhardness

Vickers's microhardness data are multiplied by an empirical number of 3.3 to convert to strength. Accordingly, the strength in ECAP-

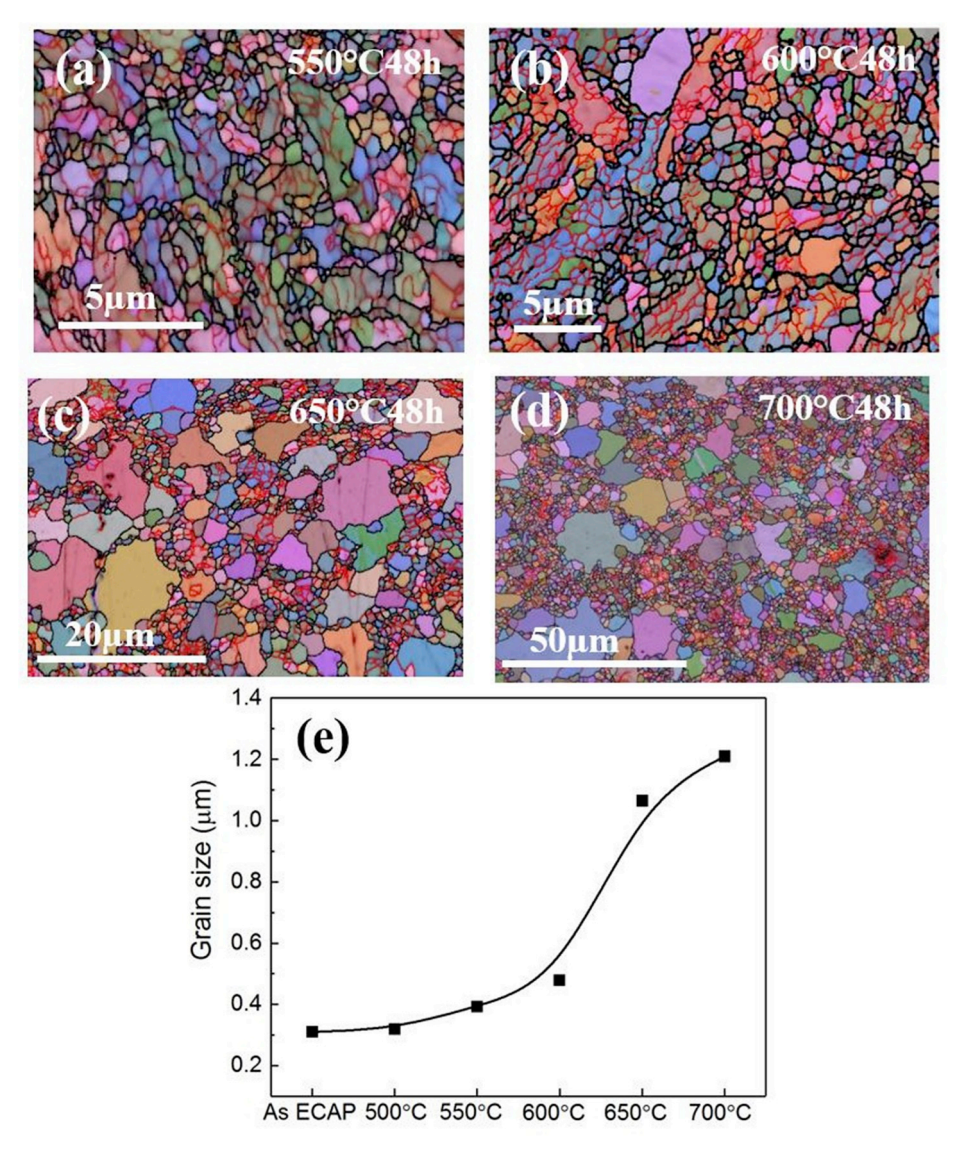
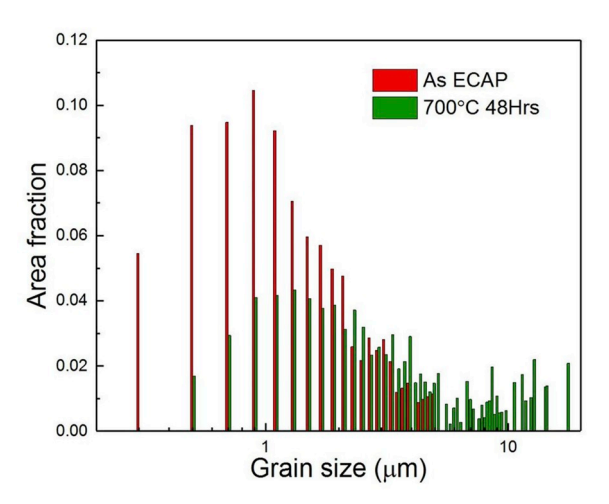


Fig. 4. EBSD orientation maps of the ECAP-processed Fe-9Cr after 48 h of annealing at (a) 550 °C; (b) 600 °C; (c) 650 °C and (d) 700 °C. The average grain size evolution after isochronous annealing at various temperatures is given in (e). Note the scale bars are different in each map.



**Fig. 5.** Comparison of grain size distributions between the as-ECAP condition and 700  $^{\circ}$ C 48h annealed condition. A bimodal grain size distribution is developed after annealing at 700  $^{\circ}$ C for 48 h.

processed condition and in 700 °C 48h annealed condition is 1033 and 617 MPa, respectively, showing a decrease of 416 MPa. A discussion is provided below to help understand the changes in strength contribution from each major strengthening mechanism operative in Fe-9Cr steel, including precipitation strengthening ( $\sigma_p$ ), dislocation strengthening ( $\sigma_d$ ), and grain boundary strengthening ( $\sigma_{gb}$ ).

As described above,  $M_{23}C_6$  precipitates coarsened, while MX precipitates remained stable during annealing. Therefore, the decrease in precipitation strengthening came from the coarsening of  $M_{23}C_6$  calculated as [32]:

$$\Delta \sigma_p = M \frac{0.4Gb}{\pi \sqrt{1 - v} \sqrt{\frac{\pi}{4F} - 1}} \left[ \frac{\ln\left(\frac{2\overline{r}_0}{b}\right)}{2\overline{r}_0} - \frac{\ln\left(\frac{2\overline{r}}{b}\right)}{2\overline{r}} \right]$$
(1)

where M = 2.7 is the Taylor factor, G = 75 MPa, b = 0.25 nm, and  $\upsilon=0.28$  are the shear modulus at room temperature, magnitude of the Burgers vector, and Poisson's ratio of the matrix, respectively. F=2.2% is the fraction of  $M_{23}C_6$ .  $\overline{r}_0=56$  nm and  $\overline{r}=85$  nm are the average radius of the cross-section of  $M_{23}C_6$  (assuming spherical) before and after annealing. After inserting the values,  $\Delta\sigma_p=19$  MPa is calculated.

Dislocation strengthening  $\sigma_d$  for bcc metals is proportional to the

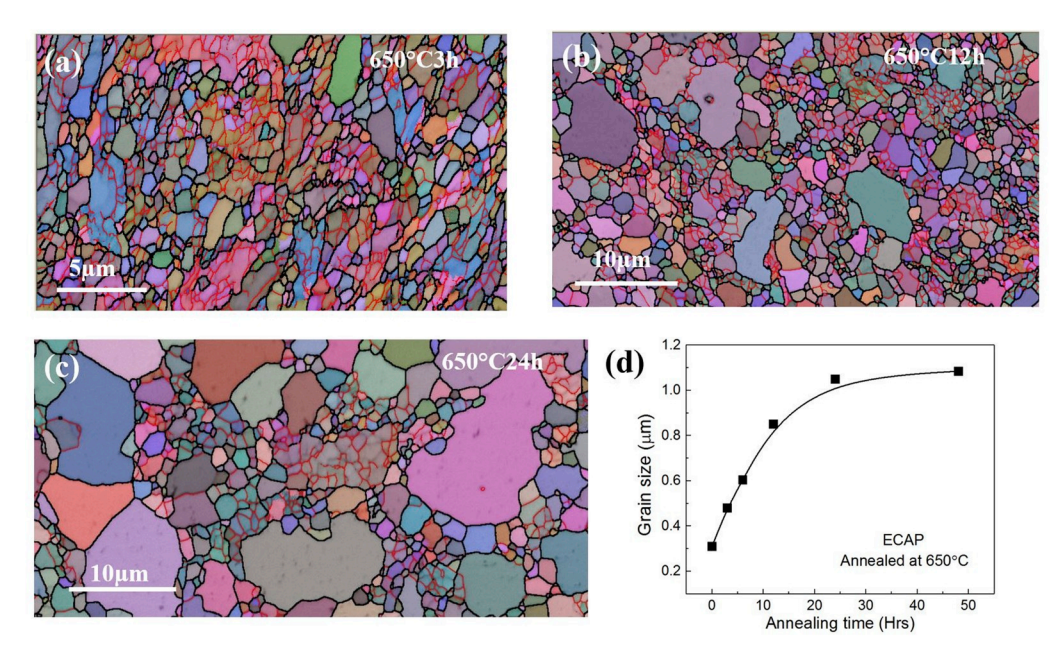


Fig. 6. EBSD orientation maps of the ECAP processed Fe-9Cr after annealing at 650 °C for (a) 3 h; (b) 12 h; and (c) 24 h. The average grain size evolution after isothermal annealing at 650 °C is given in (d). Note the scale bars are different in each map.

square root of dislocation density, and the decrease in dislocation strengthening during annealing due to a reduction in dislocation density is

$$\Delta \sigma_d = 0.5 MGb(\sqrt{\rho_0} - \sqrt{\rho}) \tag{2}$$

where  $\rho_0=2.1\times 10^{14}\,\mathrm{m}^{-2}$  and  $\rho=0.7\times 10^{14}\,\mathrm{m}^{-2}$  are the dislocation densities before and after annealing. The dislocation density,  $\rho$ , is estimated by the equation  $\rho=\frac{2\sqrt{3}\varepsilon}{d_c b}$ , where the crystalline size  $d_c$  and the micro-strain  $\varepsilon$  are determined by analyzing the XRD peak broadening with Materials Analysis Using Diffraction (MAUD) rietveld

software (XRD patterns are shown in Fig. S3). The calculated value of  $\Delta\sigma_d$  is 153 MPa.

The Hall-Petch relationship is employed to estimate the strength loss from the growth of grain size:

$$\Delta \sigma_{gb} = k \left( \frac{1}{\sqrt{d_0}} - \frac{1}{\sqrt{d}} \right) \tag{3}$$

where k is the Hall-Petch coefficient, and  $d_0$  and d are the average grain diameters before and after annealing, respectively. It is pertinent to

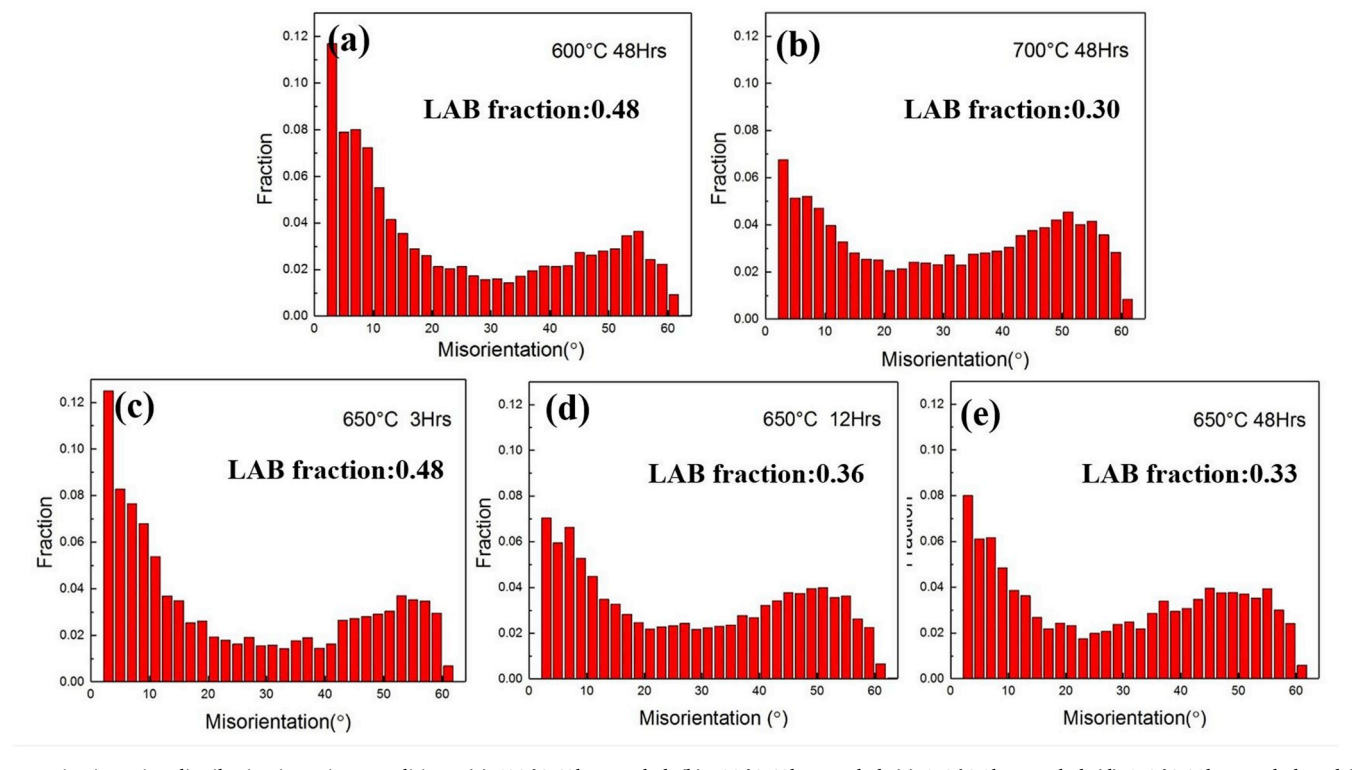


Fig. 7. Misorientation distribution in various conditions: (a) 600 °C 48h annealed; (b) 700 °C 48h annealed; (c) 650 °C 3h annealed; (d) 650 °C 12h annealed; and (e) 650 °C 48h annealed.

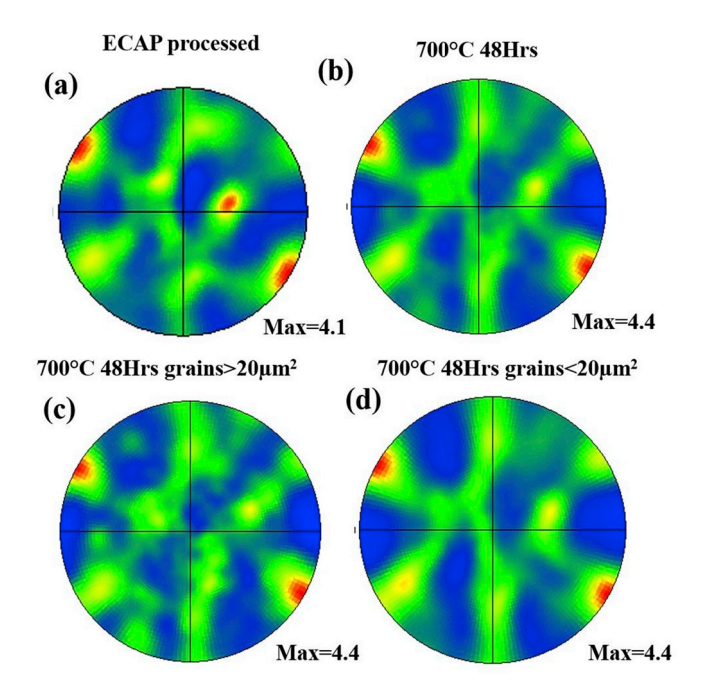


Fig. 8. (110) Pole figure for (a) as ECAP; and annealed at 700 °C for 48h: (b) all grains; (c) grains larger than  $20 \,\mu\text{m}^2$ ; and (d) grains smaller than  $20 \,\mu\text{m}^2$ .

note that the reported k value for bcc steels varies in the literature. First, different techniques, including optical microscopy, TEM, EBSD and XRD, were used to measure the average grain size, which led to discrepancies in measurements of d and the determination of k value. Second, k value may be different in different grain size ranges. Generally, k value is smaller for nano- grained steels than for CG counterparts. In a closely related review [33], results from various studies on strength of different metals, including Fe, were plotted and fitted using the Hall-Petch relationship; for Fe, k is 310 MPa  $\mu$ m<sup>1/2</sup>. If this k value is taken, a decrease of 275 MPa from grain growth is expected in the ECAP-processed Fe-9Cr after annealing for 48 h at 700 °C.

The calculated overall strength loss, due to precipitate coarsening, dislocation annihilation and grain growth, is 447 MPa, which is comparable to the experimental value (416 MPa). It is concluded that grain growth is the main reason for the strength decrease in ECAP-processed Fe-9Cr during annealing.

# 4.2. Continuous vs. discontinuous grain growth

The analytical mean field theory of annealing by Humphrey [13,34] has been widely used for understanding the annealing behavior (continuous or discontinuous grain growth) of single-phase and particle-containing metals. The theory predicts the minimum size ratio (lower bound of X,  $X_{min}$ ) required for the grain in radius R to grow in an assembly of (sub)grains in radius  $\overline{R}$ , as well as the maximum size ratio (higher bound of X,  $X_{max}$ ) that can be achieved:

$$X = \frac{R}{\overline{R}} = \frac{2\frac{M}{\overline{M}} \left(\frac{\gamma}{\overline{\gamma}} Z - 1\right) \pm 2\left[\left(\frac{M}{\overline{M}} - \frac{M}{\overline{M}} \frac{\gamma}{\overline{\gamma}} Z\right)^2 + (4Z - 1)\frac{M}{\overline{M}} \frac{\gamma}{\overline{\gamma}}\right]^{1/2}}{4Z - 1} \tag{4}$$

where

$$\overline{M} = M \left[ 1 - e^{-5} \left( \frac{\theta}{15^{\circ}} \right)^4 \right] \tag{4.1}$$

$$\overline{\gamma} = \gamma \frac{\theta}{15^{\circ}} \left( 1 - \ln \frac{\theta}{15^{\circ}} \right) \tag{4.2}$$

$$Z = \frac{3F\overline{R}}{d} \tag{4.3}$$

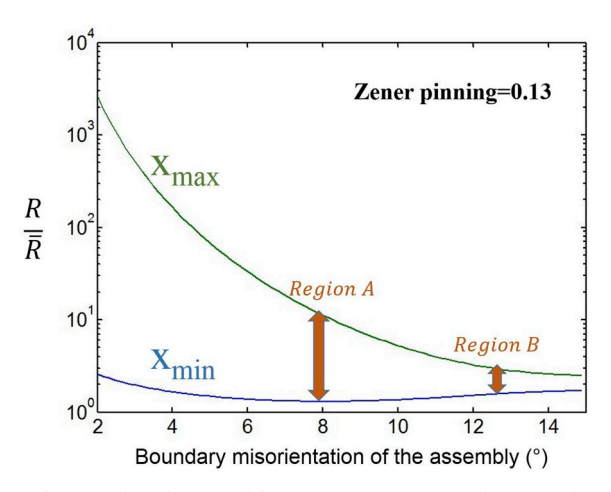


**Fig. 9.** Theoretical predictions of the size ratio a grain can achieve as a function of the mean boundary misorientation of the assembly grains. Here the influence of secondary precipitates is considered with Zener pinning = 0.13.

M and  $\gamma$  are the mobility and energy of HABs, respectively, and  $\overline{M}$  and  $\overline{\gamma}$  are the mean values for the (sub)grains assembly. Energy and mobility of LABs are functions of boundary misorientation  $\theta$  while those of HABs are considered independent of  $\theta$ . Z is the Zener pinning as a function of particle fraction F and particle size. Based on this model, a larger  $X_{max}$  value means grains would grow in a more discontinuous manner. It is reasonable to define that discontinuous grain growth occurs when  $X_{max}$  is larger than 4 [14]. The model is applied here to provide a guideline for understanding the annealing behavior of ECAP-processed Fe-9Cr, which is characterized by a heterogeneous UFG microstructure generated by ECAP. Zener pinning, associated with the effect of  $M_{23}C_6$  and MX precipitates on annealing behavior, is taken into consideration in this analysis.

In the current case, the total Zener pinning from  $M_{23}C_6$  (F=2.1%, d=116 nm),  $Z_{M_{23}C_6}$ , and MX (F=0.3%, d=40 nm),  $Z_{MX}$ , is estimated to be  $Z_{M_{23}C_6}+Z_{MX}=0.13$  with  $\overline{R}=155$  nm. The X, as a function of the mean boundary misorientation of the assembly ( $\overline{\theta}$ ), is plotted with Z=0.13 (Fig. 9). This plot shows that  $X_{max}$  is large at low  $\overline{\theta}$  and decreases as  $\overline{\theta}$  increases, suggesting discontinuous grain growth is favored at lower  $\overline{\theta}$ . In addition, as annealing leads to a considerable increase in  $\overline{R}$ , Zener pinning increases accordingly (4.3), which makes discontinuous grain growth more favorable.

It is noteworthy that the mean field model assumes the random spatial distribution of HABs and LABs, and that discontinuous grain growth occurs in a random manner. However, attention should be given to a microstructure that consists of two distinct types of regions with a heterogeneous distribution of HABs and LABs. Therefore, the annealing behavior would be different between those two regions. Since the HABs in B-type regions (Fig. 3), where HABs are dominant, possess higher driving force (higher stored energy) and higher mobility (equation (4.1)-(2)), grain growth in these regions is much faster than that in Atype regions. Based on the aforementioned model, grains in a B-type region, where  $\bar{\theta} \sim 13.5^{\circ}$ , would remain in a narrow size range during their growth, Fig. 9. After large grains eventually form from B-type regions, they will expand into A-type regions (with mainly LABs). EBSD results show  $\bar{\theta} \sim 8^{\circ}$  in A-type regions and, therefore, those large grains are expected to enjoy un-restrained discontinuous growth until they are pinned by other abnormally large grains.

# 4.3. Microstructure and grain boundary evolution

From results presented in Section 3.4 (Fig. 7), in isochronous annealing, LAB fraction increased at lower temperatures (e.g., 600 °C), but decreased at higher temperatures (e.g., 650–700 °C). In higher-temperature (e.g., 650 °C) isothermal annealing, LAB fraction increased

during the first few hours, followed by a gradual decrease as the annealing time was extended. These findings, combined with the microstructure observations, Figs. 4&6, suggest that the LAB fraction increases until discontinuous grain growth becomes evident. Therefore, the evolution of the grain boundary character was related to the microstructural changes during annealing.

It is interesting to note that the initial increase in the LAB fraction during annealing contradicts the anticipation that grain growth normally leads to its decrease. However, annealing induced an increase in the LAB fraction in some metals. Zahid et al. [16] reported the microstructure and texture of an Al with ultra-fine lamellar grains, a high fraction of HABs, and strong conventional deformation textures. In their study, upon annealing, because of the limited number of texture components, the growing grain had a high probability of encountering grains of a similar orientation, forming LABs. The fraction of LABs continued to increase throughout the whole annealing process, from coarsening and spheroidization of the lamellar grains to the growth of equiaxed grains. In the work of isothermal annealing of a high-strain cold-rolled Al by Mishin et al. [24], the LAB fraction increased during the early coarsening of the lamellar grains. However, a significant decrease of LAB fraction was accompanied by the growth of abnormal grains, mainly in P or Cube textures, which were extremely weak in a deformed condition. Because P and Cube grains shared HABs with surrounding structures in deformation textures (e.g., S, Cu, and Bs), their growth resulted in an increase in the HAB fraction. In light of the discussion, it is proposed that two conditions are required for the continuous increment in the LAB fraction during the grain growth process based on the aforementioned mechanism: (1) a limited number of strong deformation texture components; and (2) no development of so-called recrystallization texture components, such as Cube in fcc metals.

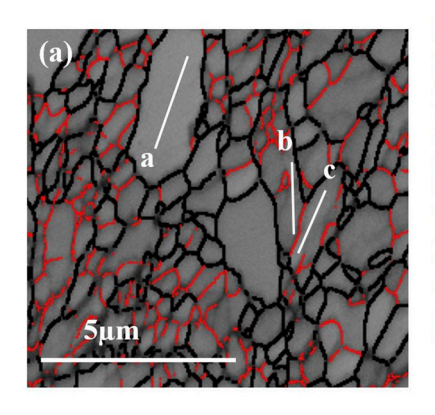
However, the aforementioned mechanism is not applicable to the increase in the LAB fraction in the current ECAP-processed Fe-9Cr during annealing. First, deformation textures are relatively weak in the ECAP-processed condition. It is known that significant strain-path changes are involved in ECAP processing when using Bc route, and strain-path change is counterproductive in developing strong textures. Therefore, during annealing, grains are less likely to encounter grains of similar orientation to form LABs. For example, Fig. 10 shows a grain (marked "a") that initiates abnormal growth and shares HABs with surrounding structural units. It appears that grain "a" is about to consume the surrounding grains that contain LABs. Meanwhile, those LABs in Fig. 10 are more likely to be the ones generated during deformation, instead of being formed during grain growth. For example, two grains (marked "b" and "c" in Fig. 10) that are sharing a LAB exhibit interior build-up of misorientation, indicating that they are deformed grains without having completed recovery yet. Therefore, the shared LAB was generated by deformation not by grain growth. Second, the absence of recrystallization textures in current case cannot explain the increase in LAB fraction during annealing. The retention of deformation textures during annealing is conducive to LABs formation only if deformation textures are strong for orientation impingement to occur. However, the deformation textures are considered relatively weak in the current case.

In our study, the evolution of grain boundary characteristics is correlated to heterogeneous grain growth. As aforementioned, grain growth proceeds faster in clusters of grains of HABs as compared to that in those subgrains of LABs. Therefore, grains of HABs will first be consumed during grain growth in B-type regions, as schematically illustrated in Fig. 11 a-b. Note that this process is less likely to generate LABs due to relatively weak textures (Fig. 10a). Meanwhile, LABs of lower mobility and lower energy are relatively stable. As a result, there is a net increase in the LABs fraction. This mechanism, which is responsible for the increase of the LAB fraction during annealing in the current case, is totally different from what was previously proposed. In the later stage, as shown in Fig. 11c, abnormal grains grow out of B-type regions and invade the A-type regions which are dominated by LABs. Resultantly, LABs from A-type regions are consumed, and the fraction of HABs increases.

#### 5. Conclusions

Thermal stability of a Fe-9Cr steel subjected to six passes of ECAP was systematically studied. The main conclusions are:

- ECAP generated near-equiaxed UFG microstructure with heterogeneous distributions of LABs and HABs. Two types of precipitates, i.e., M<sub>23</sub>C<sub>6</sub> and MX, were identified.
- 2) The microstructure was relatively stable at lower annealing temperatures (500–600 °C). Above 650 °C, discontinuous grain growth took place, resulting in a bimodal grain size distribution. Simultaneously, hardness dropped.
- 3) Partial {110} and < 111 > fibers were formed in the ECAP-processed condition. No significant change in texture was found in the annealed condition. Abnormally large grains showed textures similar to those identified in the deformed microstructures.
- 4) A mean field theory was used to explain the annealing behavior of the particle-containing microstructure. The theoretical predication agreed with the observed discontinuous grain growth in the ECAPprocessed Fe-9Cr during annealing.
- 5) For the heterogeneous microstructure, grain growth started at regions of dominantly HABs, leading to a decrease in the HABs fraction (or an increase in LABs fraction). Subsequently, the grains grew into relatively stable regions of LABs, leading to a decrease in the LAB fraction (or an increase in the HAB fraction).



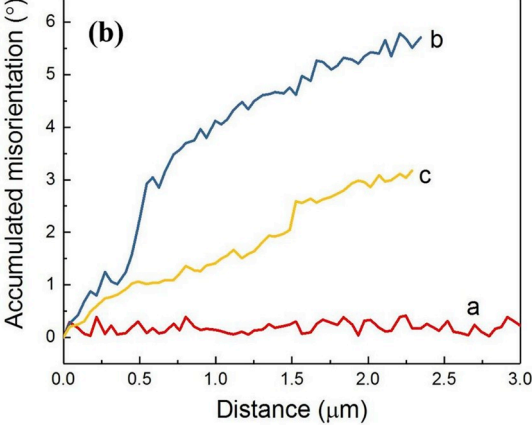


Fig. 10. (a) A typical microstructure that initiates discontinuous grain growth (after annealing at 650 °C for 3 h); (b) accumulated misorientation profile along lines within grains marked "a", "b" and "c" in (a).

Fig. 11. Schematic diagram of discontinuous grain growth in the ECAP Fe-9Cr steel during annealing: (a-b) grain growth starts from the cluster of HABs, leading to a reduction in HABs; (c) the new grain consumes the thermally stable regions of LABs.

#### Data availability statement

The raw/processed data required to reproduce these findings cannot be shared at this time as the data also forms part of an ongoing study.

## Acknowledgements

This research is financially supported by U.S. Department of Energy, Office of Nuclear Energy through the NEET-NSUF (Nuclear Energy Enabling Technology - Nuclear Science User Facility) program (award number DE-NE0008524). R. Islamgaliev is grateful to the Russian Ministry of Education for the project No. 16.2061.2017/4.6. Optimization of the ECAP regimes for processing UFG samples of steel have been supported by the RSF project No 19-19-00496. Ruslan Z. Valiev gratefully acknowledges the financial support from Saint Petersburg State University in the framework of Call 3 project (id 26130576). Part of the electron microscopy was supported by the University of Missouri Electron Microscopy Core "Excellence in Electron Microscopy" award.

# Appendix A. Supplementary data

Supplementary data to this article can be found online at https:// doi.org/10.1016/j.matchar.2019.110004.

# References

- [1] R.Z. Valiev, R.K. Islamgaliev, I.V. Alexandrov, Bulk nanostructured materials from evere plastic deformation, Prog. Mater. Sci. 45 (2000) 103-189.
- Y. Estrin, A. Vinogradov, Extreme grain refinement by severe plastic deformation: a realth of challenging science, Acta Mater. 61 (2013) 782-817.
- M. Al-Maharbi, I. Karaman, I.J. Beyerlein, D. Foley, K.T. Hartwig, L.J. Kecskes, S.N. Mathaudhu, Microstructure, crystallographic texture, and plastic anisotropy evolution in an Mg alloy during equal channel angular extrusion processing, Mater. Sci. Eng. A Struct. 528 (2011) 7616-7627.
- R.Z. Valiev, Y. Estrin, Z. Horita, T.G. Langdon, M.J. Zehetbauer, Y. Zhu, Producing bulk ultrafine-grained materials by severe plastic deformation: ten years later, Jom 68 (2016) 1216-1226.
- I.F. Mohamed, Y. Yonenaga, S. Lee, K. Edalati, Z. Horita, Age hardening and thermal stability of Al-Cu alloy processed by high-pressure torsion, Mater. Sci. Eng. A 627 (2015) 111–118.
- F.J. Humphreys, M. Hatherly, Chapter 7 recrystallization of single-phase Alloys, in: F.J. Humphreys, M. Hatherly (Eds.), Recrystallization and Related Annealing Phenomena, second ed., Elsevier, Oxford, 2004, pp. 215-IV.
- F.J. Humphreys, M. Hatherly, Chapter 2 the deformed state, in: F.J. Humphreys, M. Hatherly (Eds.), Recrystallization and Related Annealing Phenomena, second ed., Elsevier, Oxford, 2004, pp. 11–II.
- [8] H. Wen, Y. Zhao, Y. Li, O. Ertorer, K.M. Nesterov, R.K. Islamgaliev, R.Z. Valiev, E.J. Lavernia, High-pressure torsion-induced grain growth and detwinning in cryomilled Cu powders, Philos. Mag. 90 (2010) 4541-4550.
- Y.R. Kolobov, G. Grabovetskaya, M. Ivanov, A. Zhilyaev, R. Valiev, Grain boundary diffusion characteristics of nanostructured nickel, Scr. Mater. 6 (2001) 873-878.
- J. Duan, M.Z. Quadir, M. Ferry, An analytical framework for predicting the limit in structural refinement in accumulative roll bonded nickel, Metall. Mater. Trans. A 47 (2016) 471-478
- [11] X.C. Liu, H.W. Zhang, K. Lu, Formation of nano-laminated structure in nickel by

- means of surface mechanical grinding treatment. Acta Mater, 96 (2015) 24-36.
- [12] X. Liu, H. Zhang, K. Lu, Strain-induced ultrahard and ultrastable nanolaminated structure in nickel, Science 342 (2013) 337-340.
- [13] F.J. Humphreys, A unified theory of recovery, recrystallization and grain growth, based on the stability and growth of cellular microstructures—I. The basic model, Acta Mater. 45 (1997) 4231–4240.

  [14] H. Jazaeri, F.J. Humphreys, The transition from discontinuous to continuous re-
- crystallization in some aluminium alloys II annealing behaviour, Acta Mater. 52 (2004) 3251-3262.
- [15] M.Z. Quadir, O. Al-Buhamad, L. Bassman, M. Ferry, Development of a recovered/ recrystallized multilayered microstructure in Al alloys by accumulative roll bonding, Acta Mater. 55 (2007) 5438-5448.
- [16] G.H. Zahid, Y. Huang, P.B. Prangnell, Microstructure and texture evolution during annealing a cryogenic-SPD processed Al-alloy with a nanoscale lamellar HAGB grain structure, Acta Mater. 57 (2009) 3509–3521.
- T. Gladman, Second phase particle distribution and secondary recrystallisation, Scr. Metall. Mater. 27 (1992) 1569-1573.
- [18] I. Andersen, Ø. Grong, N. Ryum, Analytical modelling of grain growth in metals and alloys in the presence of growing and dissolving precipitates-II. Abnormal grain rowth, Acta Metall. Mater. 43 (1995) 2689-2700.
- [19] X. Wu, Y. Zhu, Heterogeneous materials: a new class of materials with un-
- precedented mechanical properties, Mater. Res. Lett. 5 (2017) 527–532. S.W. Wu, G. Wang, Q. Wang, Y.D. Jia, J. Yi, Q.J. Zhai, J.B. Liu, B.A. Sun, H.J. Chu, J. Shen, P.K. Liaw, C.T. Liu, T.Y. Zhang, Enhancement of strength-ductility trade-off in a high-entropy alloy through a heterogeneous structure, Acta Mater. 165 (2019)
- [21] S. Pillot, Z. Zhao, S. Corre, C. Chauvy, L. Coudreuse, P. Toussaint, Thick Plates in Grade 91 for Fourth Generation Nuclear Reactors, Pres Ves P, 2010, pp. 847–860.
- [22] R.Z. Valiev, T.G. Langdon, Principles of equal-channel angular pressing as a processing tool for grain refinement, Prog. Mater. Sci. 51 (2006) 881-981.
- [23] C. Haase, O. Kremer, W. Hu, T. Ingendahl, R. Lapovok, D.A. Molodov, Equalchannel angular pressing and annealing of a twinning-induced plasticity steel: mirostructure, texture, and mechanical properties, Acta Mater. 107 (2016) 239-253.
- [24] O.V. Mishin, A. Godfrey, D.J. Jensen, N. Hansen, Recovery and recrystallization in commercial purity aluminum cold rolled to an ultrahigh strain, Acta Mater. 61 (2013) 5354-5364.
- M. Furukawa, Y. Iwahashi, Z. Horita, M. Nemoto, T.G. Langdon, The shearing characteristics associated with equal-channel angular pressing, Mater. Sci. Eng. A 257 (1998) 328-332.
- D. Verma, S.K. Shekhawat, N.K. Mukhopadhyay, G.V.S. Sastry, R. Manna Development of texture in interstitial-free steel processed by equal-channel angular pressing, J. Mater. Eng. Perform. 25 (2016) 820-830.
- [27] S. Li, I.J. Beyerlein, M.A.M. Bourke, Texture formation during equal channel angular extrusion of fcc and bcc materials; comparison with simple shear, Mater. Sci. Eng. A Struct. 394 (2005) 66-77.
- [28] I.J. Beyerlein, L.S. Tóth, Texture evolution in equal-channel angular extrusion, Prog. Mater. Sci. 54 (2009) 427-510.
- [29] J. Duan, M. Quadir, M. Ferry, Engineering low intensity planar textures in commercial purity nickel sheets by cross roll bonding, Mater. Lett. 188 (2017) 138-141.
- [30] J. Duan, M.Z. Quadir, W. Xu, C. Kong, M. Ferry, Texture balancing in a fcc/bcc multilayered composite produced by accumulative roll bonding, Acta Mater. 123 (2017) 11-23.
- [31] J. Duan, H. Wen, C. Zhou, R. Islamgaliev, X. Li, Evolution of microstructure and texture during annealing in a high-pressure torsion processed Fe-9Cr alloy, Materialia 6 (2019) 100349.
- [32] H. Wen, T.D. Topping, D. Isheim, D.N. Seidman, E.J. Lavernia, Strengthening mechanisms in a high-strength bulk nanostructured Cu-Zn-Al alloy processed via
- cryomilling and spark plasma sintering, Acta Mater. 61 (2013) 2769–2782.

  [33] Z.C. Cordero, B.E. Knight, C.A. Schuh, Six decades of the Hall–Petch effect survey of grain-size strengthening studies on pure metals, Int. Mater. Rev. 61 (2016)
- [34] F.J. Humphreys, A unified theory of recovery, recrystallization and grain growth, based on the stability and growth of cellular microstructures-II. The effect of second-phase particles, Acta Mater. 45 (1997) 5031-5039.